Journal of The Electrochemical Society, 165 (2) H1-H9 (2018)
doi. 10.1149/2.1131802jes

Influence of a compact α-Fe_2O_3 layer on the photovoltaic performance of perovskite-based solar cells

F. Bouhjar [a, b,c], M. Mollar[a], Shafi Ullah[a], B. Marí[a] and B. Bessaïs[b]

a. *Institut de Disseny i Fabricació (IDF) - Departament de Física Aplicada, Universitat Politècnica de València, Camí de Vera s/n, 46022 València, Spain.*

b. *Photovoltaic Laboratory, Research and Technology Centre of Energy, Borj-Cedria Science and Technology Park, BP 95, 2050 Hammam-Lif, Tunisia*

c. *University of Tunis*

Abstract

In this study, uniform and dense iron oxide α-Fe_2O_3thin films are used as an electron-transport layer (ETL) in $CH_3NH_3PbI_3$-based perovskite solar cells (PSCs), in substiting the Titanium dioxide (TiO_2) ETL conventionally usedin planar heterojunction perovskite solar cells. The α-Fe_2O_3 films were synthesized using an electrodeposition method for the blocking layer and a hydrothermal method for the overlaying layer, while 2,2',7,7'-tetrakis (N, N'-di-p-methoxyphenylamine)-9,9' spirobifluorene (spiro-OMeTAD) was employed as a hole conductor in solar cells. Based on the above synthesized α-Fe_2O_3 films the photovoltaic performances of the PSCs were studied. The α-Fe_2O_3 layers were found to have a significant impact on the photovoltaic conversion efficiency (PCE) of the PSCs. This was attributed to an efficient charge separation and transport due to abetter coverage of the perovskite on the α-Fe_2O_3 films.As a result, the PCE measured under standard solar conditions (AM 1.5G, 100mW cm^{-2}) reaches5.7%.

Keywords:*α-Fe_2O_3; Electrochemical deposition; hydrothermal deposition; XRD analysis; FESEM analysis; Optical properties; photoelectrochemical properties; $CH_3NH_3PbI_3$; perovskite solar cells.*

1. Introduction:

Up until now, organometallic trihalide perovskites $CH_3NH_3PbX_3$ (X is iodine or a mixture of iodine, chlorine and bromine) have been considered as the most promising light absorption materials for solar energy conversion because of their wide absorption range [1], high extinction coefficient [2], ambipolar charge transport [3], and long electron–hole diffusion length [4]. However, recently, Perovskite-based solar cells (PSCs) have attracted increasing attention due to their superior performance and ease of fabrication. Indeed, spectacularprogress in improving the photovoltaic performance has been achieved in this field, and the power conversion efficiency (PCE) of PSCs has been greatly increased surpassing 20% [5,6 ,7 ,8 ,9 ,10].

To further understand the material properties and the mechanisms of the functioning device, simplified planar heterojunction structured devices have become the focus of many research endeavours [11]. PSCs are usually composed of a fluorine doped tin oxide (FTO) conductive substrate, a compact electron-selective layer (ESL), a mesoporous scaffold layer (optional), an organic–inorganic hybrid perovskite layer, a hole-transporting material (HTM), and a metallic electrode [12].

The quality of the ESL and perovskite layersisindispensable to get efficientPSCs [13],and plays an important role in reducing thestructural and electronic defects in the films, which in turn can significantly affect the device performance. In the case of PSCs, a lot of emphasis has been placed on perovskite film processing and alternative hole transport materials, due to the high cost of 2,2',7,7'-tetrakis-(N,N-di-p-methoxyphenamine)-9,9'-spiro-bifluorene (spiro-OMeTAD)[14].On the other hand, less attention has been paid to processing ESLs. Frequently integrated in PSCs as a promising ESL material, TiO_2 is a semiconductor with a wide band gap [15,16,17,18,19,20]. However, TiO_2 has low electron mobility, which might create unbalanced charge transport in the perovskite [21]**.** Besides, this compact layer often requires high temperature sintering at 450–500°C prior to use [22,23,24]making it incompatible with flexible substrates and easy fabrication. Indeed,Snaith et al.[14]suggested by that oxygen vacancies in the TiO_2 electrode are activated by UV light, which increase charge traps causing the degradation of the PCEs of the PSCs. Therefore, many efforts have been doneto use other n-type inorganic nanocrystals as alternative electron conductors in PSCs.

Several n-type inorganic nanocrystals such as ZnO, SnO,CdSe, CdS and α-Fe_2O_3 have been considered as possible substitute of TiO_2, and have displayed considerable power conversion efficiency [25,26,27,28,29,30]**.** Among all the alternative materials, α-Fe_2O_3 has been widely used as

Journal of The Electrochemical Society, 165 (2) H1-H9 (2018)
doi. 10.1149/2.1131802jes

an anode material for supercapacitors [31]. Itis one of the most common n-type materials, and the most stable iron oxide with n-type semiconducting properties under ambient conditions. It has been used as photoanode indye-sensitized solar cells to enhance the electron transfer rate[32], however its useas an electron transporting replacing TiO_2 has not yet been reported. Thus, we employed low cost α-Fe_2O_3 for the first time as the ETL material instead of TiO_2 in planar perovskite cells. The charge accumulation at the perovskite/α-Fe_2O_3 interface is significantly reduced and hence is prominently effective in reducing the hysteresis. Furthermore, the fabricated solar cells showa good stability upon exposure to ambient air without any encapsulation.The studied materials for perovskite solar cells are $CH_3NH_3PbI_3$, $CH_3NH_3PbI_{3-x}Cl_x$, $CH_3NH_3PbBr_3$,$CH_3NH_3Pb(I_{1-X}Br_x)_3$, $HC(NH_2)_2PbI_3$,$HC(NH_2)_2Pb(I_{1-X}Br_x)_3$, and $CH_3NH_3SnI_3$. In Table 1, the reported performances are summarized in terms of material $CH_3NH_3PbI_3$ and cell configuration.HTM materials are also important for high efficiency perovskite solar cells, where the most studied HTM is spiroMeOTAD,but polymertic HTMs such as the thiophene derivative P3HT and tryarylamine-based PTAA have also been tested. In addition, inorganic HTMs such as NiO, CuI, and CuSCN are confirmed to be suitable for perovskite solar cells.

Materials	Cell configuration	J_{sc} [mA/cm2]	V_{oc} [V]	FF	PCE (%)	Ref
$MAPbI_3$	mesoporous-TiO_2/$MAPbI_3$/spiro-MeOTAD	17.6	0.888	0.62	9.7	[33]
	$MAPbI_3$/PCBM	10.32	0.60	0.63	3.9	[34]
	mesoporous-TiO_2/$MAPbI_3$/P3HT-MWNT	14.8	0.76	0.57	6.45	[35]
	rutile TiO_2 nanorod/$MAPbI_3$/spiro-MeOTAD	15.6	0.955	0.63	9.4	[36]
	mesoporous-ZrO_2/$MAPbI_3$/spiro-MeOTAD	17.3	1.07	0.59	10.8	[37]
	NiO/MAPbI $_3$/PCBM	13.24	1.040	0.69	9.51	[38]
	mesoporous-TiO_2/$MAPbI_3$/CuI	17.8	0.55	0.62	6.0	[39]
	Fe_2O_3/$MAPbI_3$/ spiro-MeOTAD	11.27	1.55	0.33	5.7	our work

Table 1. Photovoltaic performance of perovskite ($MAPbI_3$) solar cells. J_{sc}, V_{oc} and FF stand for short-circuit current density, open-circuit voltage, and fill factor,respectively.

The present report mainly focuses on the deposition of a compact α-Fe_2O_3 film, and its impact on the growth of the perovskite layer, providing a comprehensive understanding of the properties of the α-Fe_2O_3/perovskite interface. The α-Fe_2O_3 films are fabricated using an electrodeposition method for the blocking layer and a hydrothermal method for the overlying layer. Then the as-synthesized α-Fe_2O_3 films are used for PSCs. The impact of the growth of the α-Fe_2O_3 film on the properties of the α-Fe_2O_3/perovskite interface and on the performance of PSCs is investigated. Morphologically uniform α-Fe_2O_3 film let's achieve a PCE of 5.7%.These results show the application possibility of α-Fe_2O_3 in PSCs, and provide the principle for the choice of the electron transport layer for efficient PSCs.

2. Experimental details

2.1. Synthesis of α-Fe_2O_3 thin films

2.1.1. Under layer fabrication (α-Fe_2O_3 (A))

The experimental set-up used to prepare α-Fe_2O_3thin films consistsof a computer-controlled potentiostat/galvanostat and a classic threeelectrodes electrochemical cell. The electrochemical cell was filled with a solution containing 5mM $FeCl_3$ +5mM KF+ 1M H_2O_2 +0.1M KCl as supporting electrolyte in deionized water. The working electrode is a substratecomposed offluorine-doped tin oxide (FTO) coated glass havinga sheet resistance of 10 Ω;the previous substrate iscleaned in an ultrasonic acetone bath for 10 min, then rinsed in distilled water and dried. Pt and Ag/AgCl electrodes were used as a counter electrode and a reference electrode, respectively. Thefilmswere deposited by cathodic electrodeposition. The deposition potential was fixed at - 0.15 V and the deposited charge was 1.2 C for all samples in order to have a thickness of approximately 40-60 nm for all Fe_2O_3films. A thermostat fixed the solution temperature at 298K. After deposition, the films were rinsed with distilled water. To obtain the desired α-Fe_2O_3phase, the deposited films were annealed in air at 650°C for 2h. The transition between phases, from β-FeOOH (yellow) to **α**-Fe_2O_3 (red–brown) is shownin figure 1.

Journal of The Electrochemical Society, 165 (2) H1-H9 (2018)
doi. 10.1149/2.1131802jes

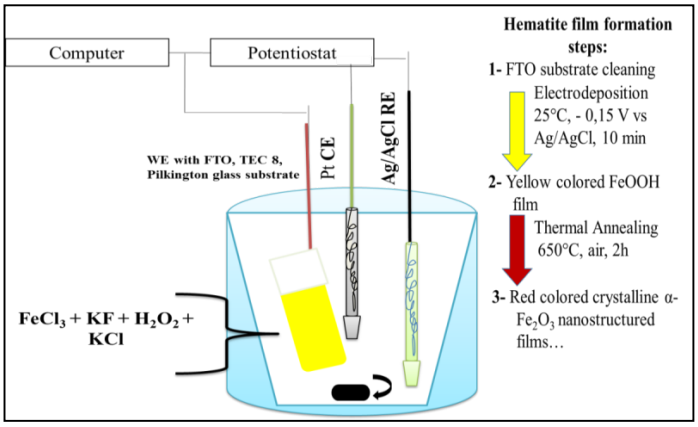

Figure 1: Schematic representations of a typical three-electrode electrochemical cell

2.1.2. On layer fabrication (α-Fe_2O_3 (B))

Nanostructured **α**-Fe_2O_3 (B) thin films were obtained after annealing hydrothermally deposited iron films on a smooth α-Fe_2O_3 surface (A). The bath was done by filling a 30-mL recipient, with a 20-mL aqueous solution containing 0.15 M of $FeCl_3.6H_2O$ and 1 M $NaNO_3$ at pH 1.5 (adjusted by HCl), leading to the deposition of iron hydroxides (FeOOH). Iron films were deposited on the **α**-Fe_2O_3 (A) substrate from an iron precursor solution ($FeCl_3.6H_2O$). [40,41,42]. A piece of FTO/**α**-Fe_2O_3 (A) was put into the autoclave, then heated at 100°C for 6h and naturally cooled down to ambient temperature.Under hydrothermal conditions, this solution enables the interaction of Fe^{3+} ions with OH^-, producing iron oxide nuclei, as described by Eq. (1):

$$\mathbf{Fe^{3+}_{(aq)} + 3OH^-_{(aq)} \rightarrow \beta\text{-}FeOOH_{(s)} + H_2O_{(l)}}$$

As a result, a uniform layer of β-FeOOH grows on the FTO substrate. The akageneite-coated substrate was then washed with deionized water and subsequently sintered in air at 550°C for 4 hours. Duringthe annealing process, the β-FeOOH converts into α-Fe_2O_3.The phase transition from β-FeOOH (yellow) to **α**-Fe_2O_3 (red–brown) is shown in figure 2. During the phase transition, the occurringchemical reaction is due to the thermal treatment, it can be represented by Eq. (2):

$$\mathbf{2\beta\text{-}FeOOH_{(s)} \rightarrow Fe_2O_{3(s)} + H_2O_{(L\ or\ G)}\ (2)}$$

Journal of The Electrochemical Society, 165 (2) H1-H9 (2018)
doi. 10.1149/2.1131802jes

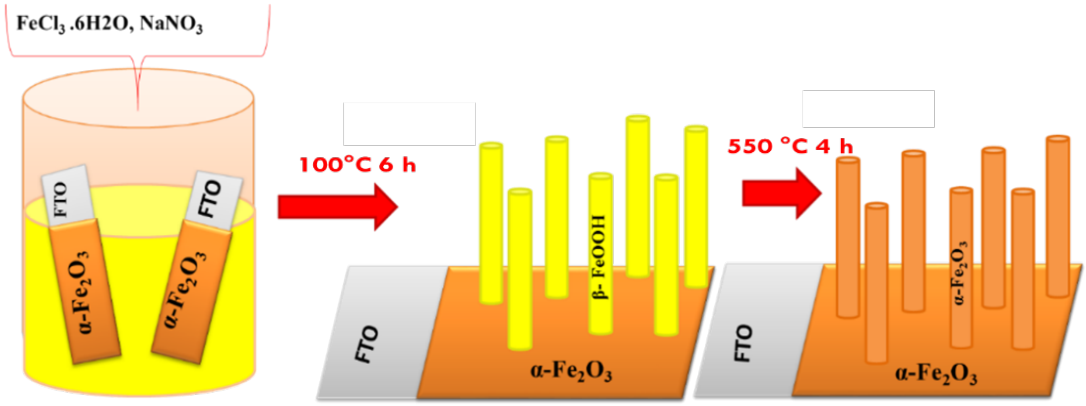

Figure 2: Schematic representations of the syntheses methods adopted for α-Fe_2O_3hematite photoanode film electrodeposited on α-Fe_2O_3(A) substrate.

2.2. fabrication of the perovskite-based Solar cell ($CH_3NH_3PbI_3$ or $MAPbI_3$)

The $MAPbI_3$ perovskite precursor solution was prepared from an equi-molar of Methylammonium iodide (CH_3NH_3I or MAI)/Lead (II) iodide(PbI_2), in a 40%dimethylformamide (DMF) solution with ratios 1:1 (1:1 mol %) for MAI: PbI_2 and then stirred for 2h at 70 °C. The mixture was deposited onto (FTO) covered glass by spin-coating at 3500 rpm for 11 s. A drop of toluene was added after 2-4 s before the end then dried at 5000 rpm for 30s.The resulting perovskite layers were then annealed at 100°C for 1h. Before the deposition process, the FTO glass substrates were cleaned with ethanol, isopropanol, and water for 15 min, and then dried with clean dry air. The reactionresults in the formation of a compact and flatcrystalline MAI-DMFPbI2 intermediate phase film.

$$PbI_2\text{-}MAI\text{-}DMF \rightarrow MAPbI_3 + DMF\uparrow \quad (3)$$

The intermediate phase film is successfully converted into acrystalline perovskite film by annealing at 100 °C, as shown in Eq. (3). The DMF is removed in the intermediate phase film, leavinga compact and flatmorphology (Fig. 3).

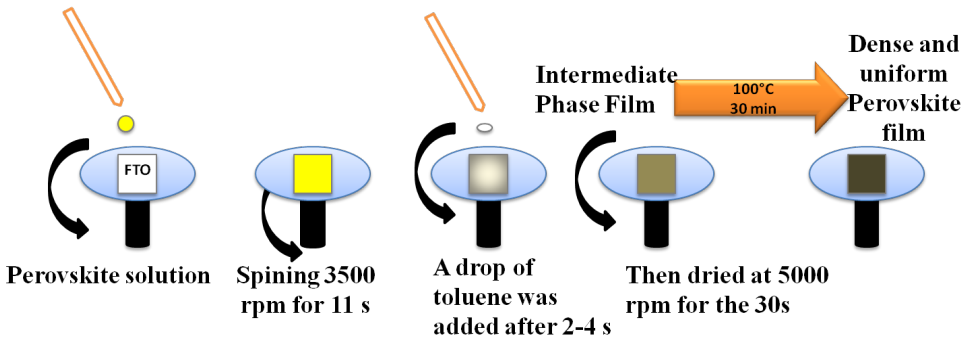

Figure 3: Solvent engineering procedure for preparing the uniform and dense perovskite film

Journal of The Electrochemical Society, 165 (2) H1-H9 (2018)
doi. 10.1149/2.1131802jes

The hole-transporting layer (HTM) was then deposited via spin-coating using a 0.788M solution of 2,2',7,7'-tetrakis-(N, N-di-p-methoxyphenylamine)9,9'-spirobifluorene (spiro-OMeTAD) in chlorobenzene, with additives of 0.0184M lithium bis (trifluoromethanesulfonyl) imide (added in 0.61M acetonitrile solution) and 0.0659M 4-tert-butylpyridine. The HTM was spin coated at 4500 rpm for 30 s inside adrybox. Finally,the top anode (a 50 nm-thick gold (Au) film)contact was deposited by thermal evaporation under a vacuum of ~10^{-6}Torr, yielding an active area of 0.2 cm^2, to complete the creation of the device (inset in Fig. 4).

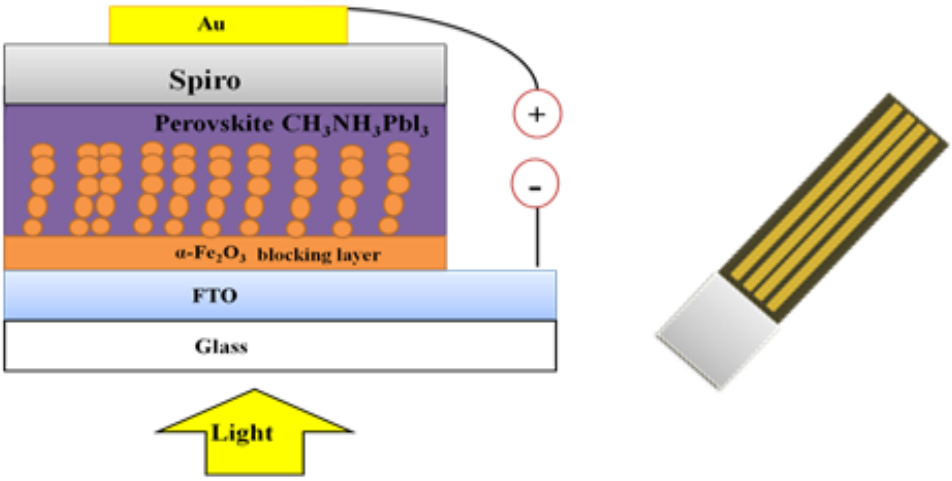

Figure4: Schemeof the perovskite solar cell

3. Results and discussion

3.1. Structural characterization

The crystal structure of α-Fe_2O_3 and α-Fe_2O_3/perovskite thin films wasinvestigated by X-ray diffraction (XRD) using a Rigaku Ultima IV diffractometer in the Bragg-Bentano configuration (the X-ray radiation is $\lambda_{CuK\alpha}$= 1.54060 Å). Figure 5 (a) shows the XRD patterns of α-Fe_2O_3(A), α-Fe_2O_3(B) and a α-Fe_2O_3/α-Fe_2O_3bilayer deposited on FTO substrates. The diffractograms of the α-Fe_2O_3/α-$Fe_2O_3$and the FTO substrates are also shown.The XRD linesof the α-Fe_2O_3films are observed at 2θ = 24.1°, 33.1°, 35.6°, 40.9°, 49.4°, 54.0° and 64°, corresponding to the (012), (104), (110), (113), (024), (116) and (300) planes of the hematite phase, respectively. The dominant linescorrespond to the (104) and (110) planes. The diffraction linesof the trigonal structure of α-Fe_2O_3matches well with the reference pattern of

Journal of The Electrochemical Society, 165 (2) H1-H9 (2018)
doi. 10.1149/2.1131802jes

the JCPDS card file n°33-0664, which corresponds to the space group R3c (167) with lattice parameters a=b=5.03 nm and c= 13.74 nm.

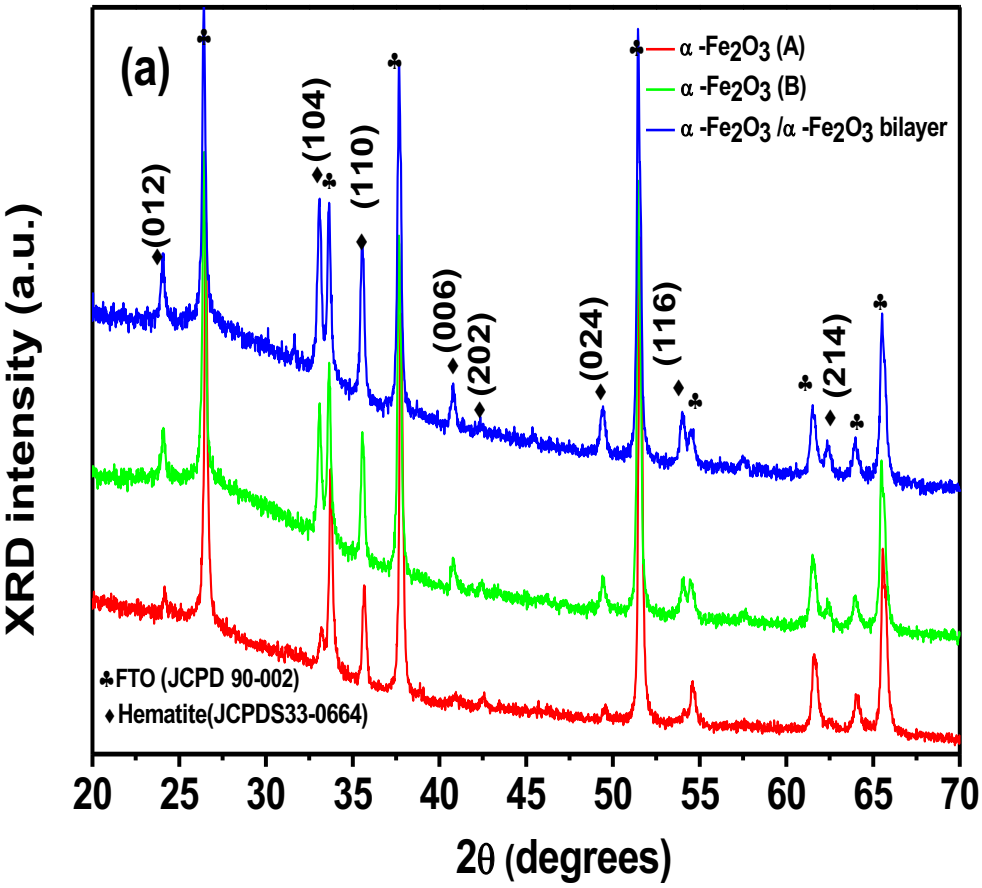

Figure 5 (a) XRD spectra of α-Fe_2O_3(A), α-Fe_2O_3(B) andα-Fe_2O_3/α-Fe_2O_3bilayer.

Figure 5 (b) shows the X-Ray diffractograms for the $MAPbI_3$ and α-Fe_2O_3 (A)/α-Fe_2O_3 (B)/ $MAPbI_3$/FTO thin films. XRD linesare located at 15°, 20°, 24.4°, 28.4°, 31.8°, 40.6° and 43°. $MAPbI_3$ thin films crystallize and stabilize into the same cubic structure (Fig. 5 (c)). The most intense diffraction line located below 15° corresponds to the (100) diffraction plane and the lineslocatedat about 20°, 30° and 34° are related to the (110), (200) and (210) orientation planes, respectively. One may also observe two diffraction lines located at 26.5° and 33.7°corresponding to the FTO substrates. For the α-Fe_2O_3 (A)/α-Fe_2O_3 (B)/$MAPbI_3$/FTO layers, all linesmatch the α-Fe_2O_3 (A), α-Fe_2O_3 (B), and $MAPbI_3$ patterns except those marked with a solid dark pointthat come from the FTO substrate.

Journal of The Electrochemical Society, 165 (2) H1-H9 (2018)
doi. 10.1149/2.1131802jes

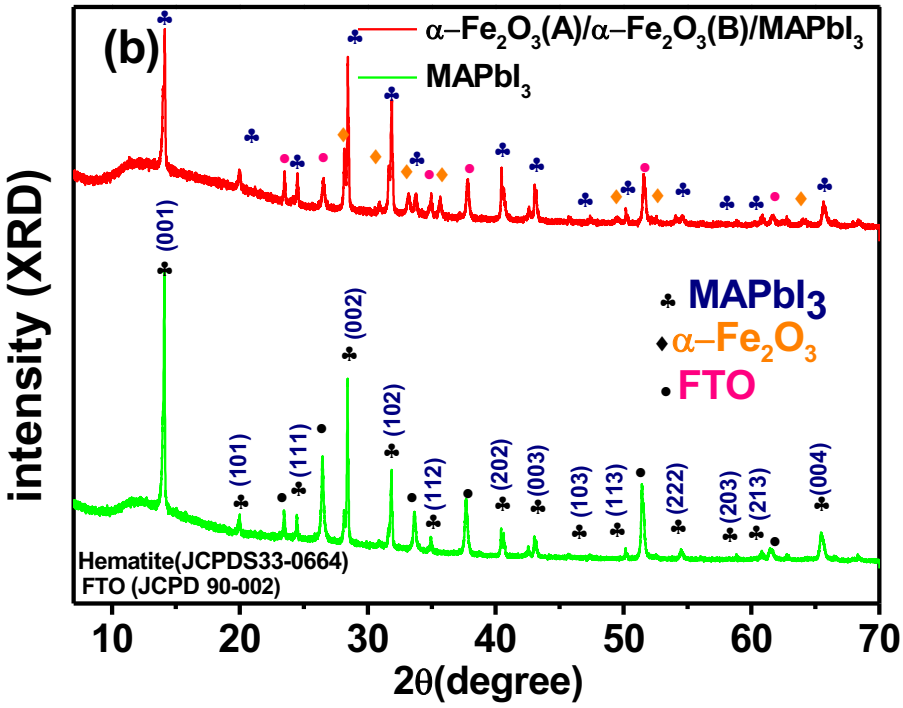

Figure 5 (b).XRD patternsof $MAPbI_3$ andα-Fe_2O_3(A)/α-Fe_2O_3(B)/$MAPbI_3$/FTO.

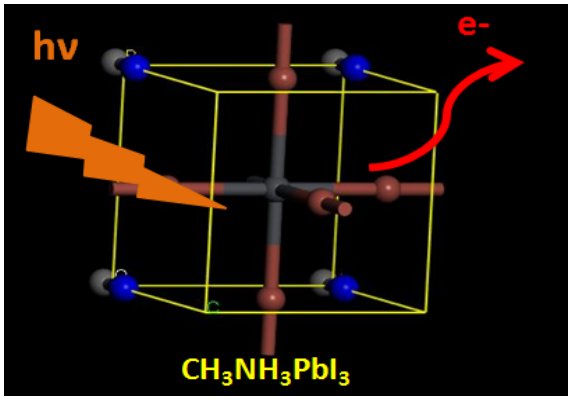

Figure 5 (c). Schemeof $MAPbI_3$ perovskite crystallization

3.2. Morphological characterization

The microstructural and elemental analyses were characterized using a Zeiss ULTRA 55 model scanning electron microscope (FESEM) equipped with an energy dispersive spectroscopy (EDS) system. Figure 6 displays the FESEM images of (a) α-Fe_2O_3 (A), (b) α-Fe_2O_3 (B), (c) α-Fe_2O_3(A)/α-Fe_2O_3(B), (d) $MAPbI_3$, (e) α-Fe_2O_3 (A)/α-Fe_2O_3(B)/$MAPbI_3$ and (f) the solar cell deposited on FTO substrates, respectively. Figure 6 (a) shows vertically grown segregated nanostructured islands made up of small Fe_2O_3(A) nanoparticles,

Journal of The Electrochemical Society, 165 (2) H1-H9 (2018)
doi. 10.1149/2.1131802jes

showingsome grain sizedispersion. Figure 6 (b)shows the microstructure of the as-prepared sample. The llater allows us to point outthe formation of typical anisotropic-like nanoparticles, mainly composed of nanostructured rods, which is a characteristic of the mesoporous film. Figure 6 (c) depicts the morphology of α-Fe_2O_3/α-Fe_2O_3bilayer thatreveals nanostructured aggregates havingagrain size of approximately 20 nm. The α-Fe_2O_3(B) grains deposited on α-Fe_2O_3(A)are larger than those deposited on FTO.Figure 6 (d) shows that the $MAPbI_3$ film is composed of dense and homogenous fibre-like crystals with the presence of voids due to solvent evaporation.Figure 6 (e) shows that the fibre-like $MAPbI_3$ films deposited on α-Fe_2O_3(A)/α-Fe_2O_3(B) have dissimilar shapes and sizes.Figure 6 (f) shows the α-Fe_2O_3(A)/α-Fe_2O_3(B)/$MAPbI_3$/spiro-OMeTAD/Au, where the $MAPbI_3$ film becomes uniform with a denser morphology.Figure 7 shows the vertical cross section of the FESEM image of the entire structure (α-Fe_2O_3 (A)/ α-Fe_2O_3 (B)/ $MAPbI_3$/spiro-OMeTAD/Au) deposited on FTO. The thickness of the cell is about 4.8μm and the thickness of the α-Fe_2O_3/α-Fe_2O_3bilayer is about 258 nm (Fig. 7.b).

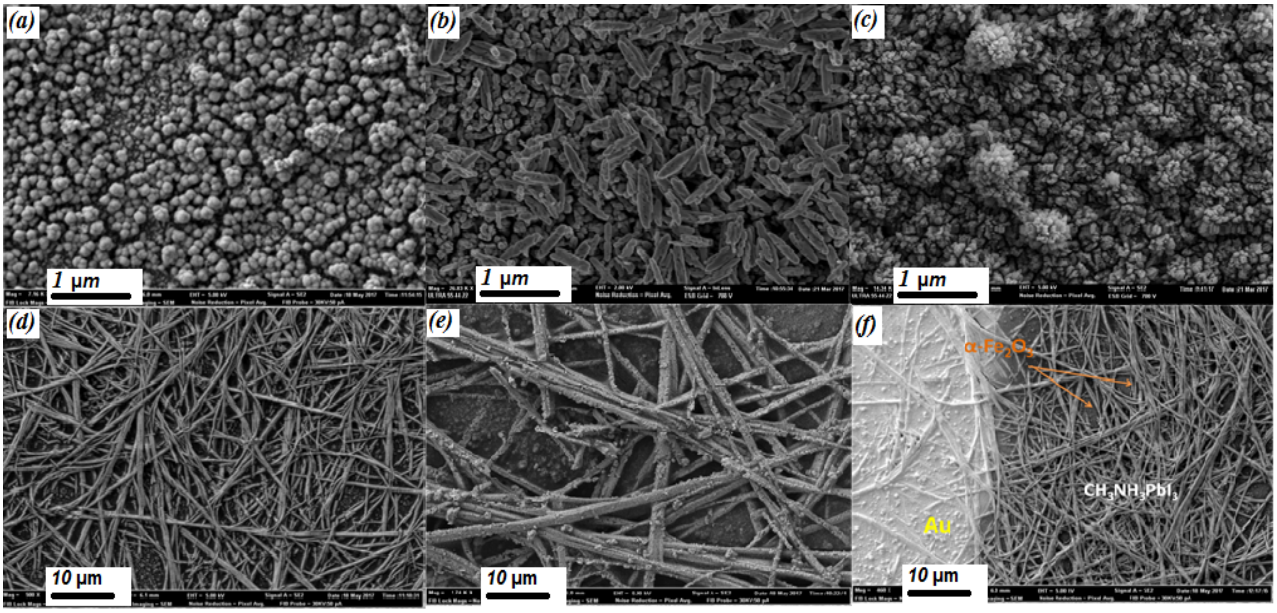

Figure 6: FESEM images of(a) α- Fe_2O_3(A), (b) α-Fe_2O_3(B) ,(c) α- Fe_2O_3(A)/α-Fe_2O_3(B),(d)$MAPbI_3$,(e) α-Fe_2O_3(A)/α-Fe_2O_3(B)/$MAPbI_3$ and (f)solar cell.

Journal of The Electrochemical Society, 165 (2) H1-H9 (2018)
doi. 10.1149/2.1131802jes

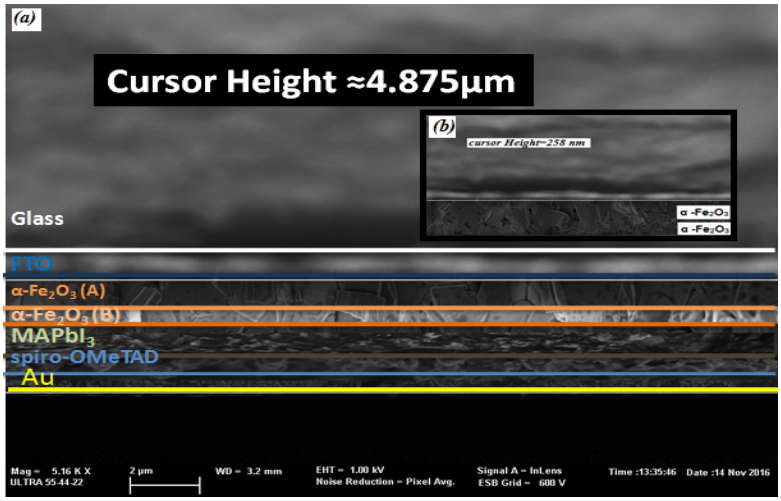

Figure 7: Vertical cross section of (a) α-Fe_2O_3(A), (b) α-Fe_2O_3/α-Fe_2O_3 thin films.

3.3. EDX analyses

Figure 8.A shows a EDX elemental analysis of the deposited $MAPbI_3$, α-Fe_2O_3(A)/α-Fe_2O_3(B), α-Fe_2O_3(A)/α-Fe_2O_3(B)/$MAPbI_3$. The line observed at 0.72 keV corresponds to the L line of Fe, and the oxygen K line is peaking at 0.525 keV. The calculated atomic ratio of Fe and O is approximately equal to 2:3, whichwell agrees with the stoichiometric composition of α-Fe_2O_3. The percentage of each element was calculated from EDX analyses (Fig. 8).The element ratio of the $MAPbI_3$ film is shown in Figure 8.A (a);two featured lines peaking at 2.48 and 3.98 keV are assigned to the Pb and I elements, respectively.The EDXpresented in Fig.8.A (a) shows that Pb and I are well distributed on a large energy scale. Figures 8.A (c-d) show the elemental composition of the solar cell and confirm the presence of each element formingthe cell. The line observed at 2.3 keV corresponds to the M line of the gold (Au) contacts.

Journal of The Electrochemical Society, 165 (2) H1-H9 (2018)
doi. 10.1149/2.1131802jes

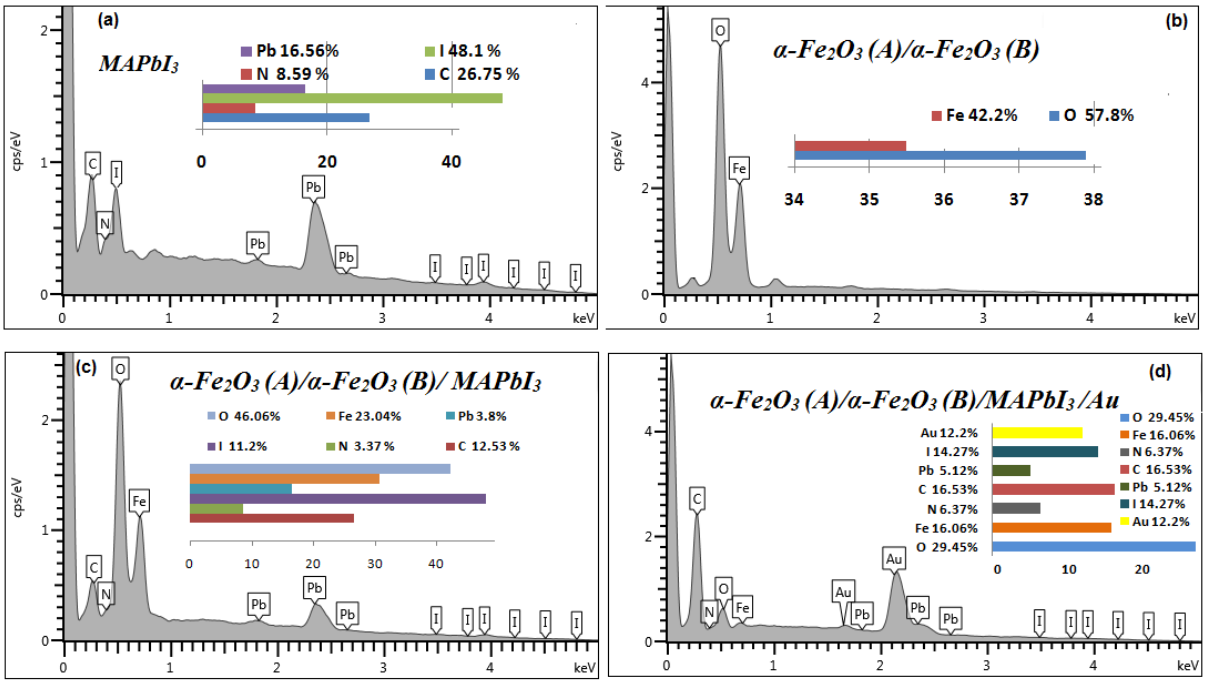

Figure 8.A : EDX spectrum for(a)$MAPbI_3$, (b) α-Fe_2O_3(A)/α-Fe_2O_3(B),(c) α-Fe_2O_3(A)/α-Fe_2O_3(B)/$MAPbI_3$, and(d)solar cell.

Figure 8.B showsthe spatial distribution ofα-Fe_2O_3+$MAPbI_3$, where Pb and I are three-dimensionally well-distributed in the α-Fe_2O_3 film. The atomic percentage calculated from the EDX analyses indicates that the Pb to I ratio is 1:3. Compared to the Fe atomic ratio, Pb has a relatively lower atomic percentage indicating that the perovskite sensitizer doesnot densely cover theα-Fe_2O_3 surface.It can be concluded that the α-Fe_2O_3composites can uniformly encapsulate the $CH_3NH_3PbI_3$ crystals.

Journal of The Electrochemical Society, 165 (2) H1-H9 (2018)
doi. 10.1149/2.1131802jes

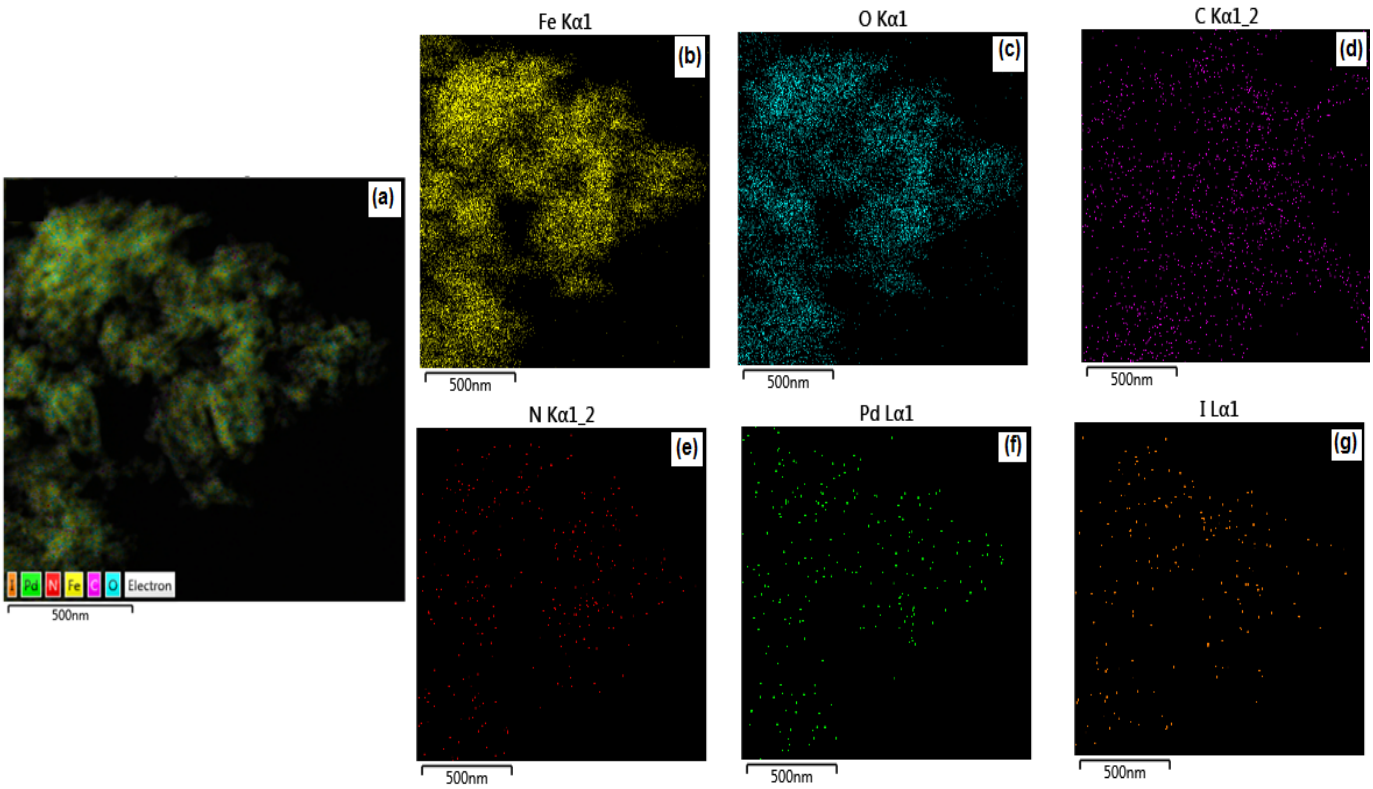

Figure 8 B: EDX mapping for(a)α-Fe_2O_3(A)/α-Fe_2O_3(B)/$MAPbI_3$,(b)Fe map, (c)O map, (d) C map, (e) N map, (f) Pb map and (g) I map.

3.4. Optical characterization of α-Fe_2O_3 thin films

The band gap energy was determinedfrom the optical absorption by recording the transmission spectra using a UV-Visible spectrophotometer (Ocean Optics HR4000) coupled with an integrating sphere (to collect both specular and diffuse transmittance). Figure 9 shows the transmission spectra of the α-Fe_2O_3/α-Fe_2O_3 bilayer, from which the optical band gap energies can be determined. The transmittance spectrum of the α-Fe_2O_3/α-Fe_2O_3 bilayer shows a high optical transmission ratio: above 30% in the visible range. A significant increase in absorption below 533 nm can be assigned to the intrinsic band gap absorption of the α-Fe_2O_3/α-Fe_2O_3 bilayer. To calculate the optical band-gap energy (E_g) of the films, the absorption coefficient can be estimated as follows: [43]

$$\alpha = \frac{1}{d} \ln \left(\frac{1}{T}\right) \qquad (4)$$

According to the solid band theory, the relation between the absorption coefficient **α** and the energy of the incident light ***hν*** is given by:[44]

$$\alpha h\nu = A\,(h\nu - Eg)^{n} \qquad (5)$$

Journal of The Electrochemical Society, 165 (2) H1-H9 (2018)
doi. 10.1149/2.1131802jes

Where ***α*** is the absorption coefficient, ***A*** is a constant, ***h*** is the Planck's constant, ***ν*** is the incident photon frequency, ***Eg*** is the optical band gap, and ***n*** is equal to 2 for a direct transition, and to 1/2 for an indirect transition. Figure 9 depicts the Tauc plot of α-Fe_2O_3/α-Fe_2O_3 bilayer. One may point out a direct band gap energy of about 2.3 eV, smaller than that of bulk α-Fe_2O_3 (2.3 eV).

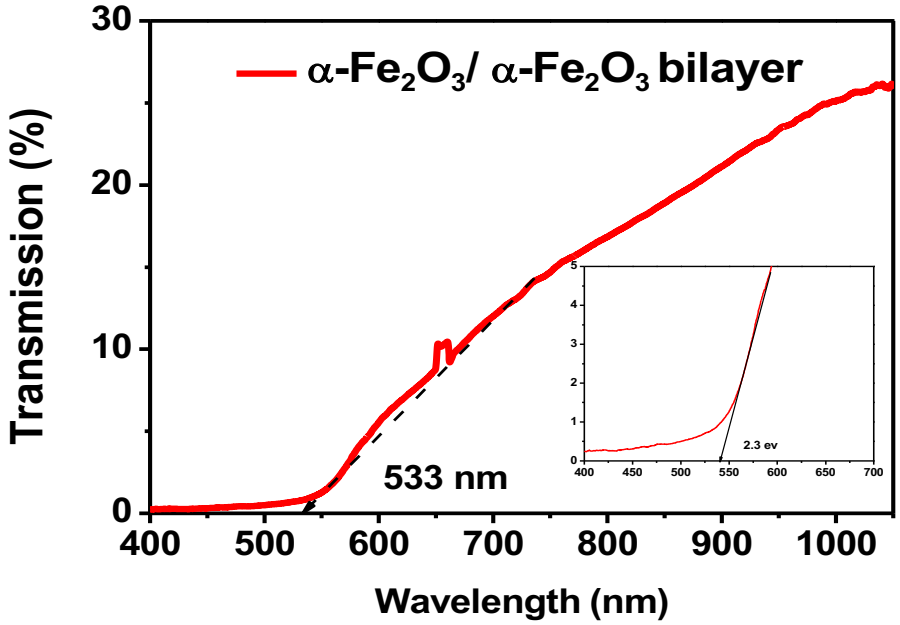

*Figure 9: Transmission and Tauc plot (inset) of α-Fe_2O_3/α-Fe_2O_3*bilayer

Figure 10 shows the transmissionand the absorbance of theMAPbI_3 perovskitethin film. The main features of the transmissionspectra arethe existence of a sub-band gap absorption tail followed by astrong rise of the absorption, which corresponds to excitonicabsorption, and then a transition from the valence band to theconduction band. When excitonic absorption dominates theabsorption spectrum, the classical relationship between the coefficients (α) and the band gap energy (Eg) is commonly used for calculating the direct band gap of a semiconductor:

$$(\alpha.h\nu)^2=A(E-Eg) \qquad (6)$$

where E is the incident photon energy and A is a constant [45].One may point out a direct band gap energy of about 1.58eV.

Journal of The Electrochemical Society, 165 (2) H1-H9 (2018)
doi. 10.1149/2.1131802jes

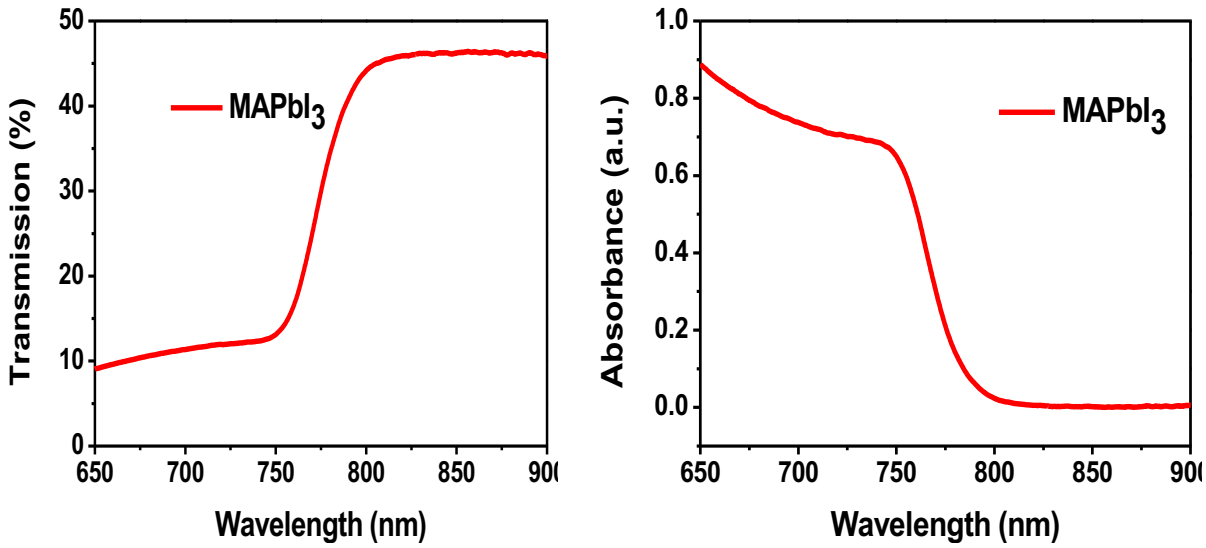

Figure 10:Transmission and Absorbanceplotsof perovskite thin films.

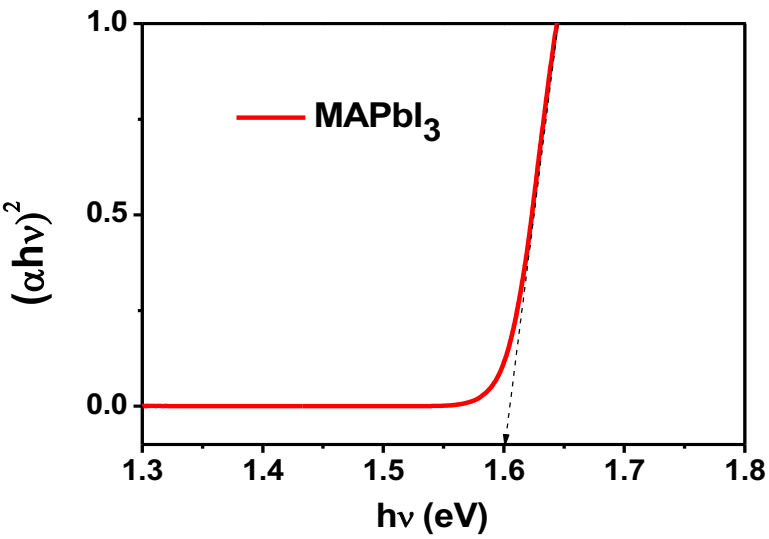

Figure 11: Tauc plot of the perovskite thin films.

3.5. Photoelectrochemical properties of α-Fe_2O_3electrodes.

The PEC measurements were performed in a quartz cell to enable light reaching the photoelectrode surface. The surface area of the light-exposed working electrode was about 0.25 cm^2. The electrolyte used in all PEC measurements is 1M NaOH (pH = 13.6). The electrolyte is purged with nitrogen gas prior to experiments to prevent any possible reaction with dissolved oxygen at the counter-electrode. A potentiostat/galvanostat Autolab PGSTAT302N (Metrohm, Netherlands) with a Pt rod counter electrode and an Ag/AgCl saturated in 3 M KCl reference electrode was used. The films are illuminated with a 300 W Xenon lamp (PLSSXE300/300UV) equipped with a UV cut-off filter (λ> 420 nm). The set-up

was completed with an automatic shutter and a filter box. The whole system was controlled by homemade software. The chronoamperometry curves of the films were also obtained at +0.1 V, both in the dark and under illumination with a light intensity of about 1 SUN (100 mW cm^{-2}) at the sample surface.

For wavelength-dependent photocurrent measurements a monochromator giving a ~20 nm bandpass from 360 to 680 nm was used together with cut off filters to eliminate secondary - harmonics. The incident photon to electron conversion efficiency (IPCE) of the samples was calculated as follows:

$$\mathbf{IPCE}(\%) = \frac{\mathbf{1240} \cdot i_{photocurrent}\ (\mu\mathrm{A}/cm^2)}{\lambda(\mathrm{nm}) \cdot j_{photons}\ (\mu W/cm^2)} * \mathbf{100\%(7)}$$

The photocurrent density–voltage (J–V) characteristics of theα-Fe_2O_3(A)/α-Fe_2O_3(B)/$MAPbI_3$ solar cell were registered using a potentiostat/galvanostat Autolab PGSTAT302 under AM 1.5G illumination (50 mW cm^{-2}) providedby a calibrated solar simulator (using a standard silicon solar cell before measurement).

The photocurrent intensities under pulsed light were measured using a chronoamperometric technique (Fig. 12). All measurements were made in 1M NaOH [46,47] electrolyte and under a potential bias of 0.1 V. Figure 12 shows the variation of the photocurrent density according to the elapsed time during on/off cycles. In the steady state, the α-Fe_2O_3(A)/FTO electrode shows a photocurrent density of about 3mA/cm^2. However, the α-Fe_2O_3/α-Fe_2O_3/FTO bilayer shows a photocurrent density of about 12mA/cm^2, which is 4and 2 times greater than that of the α-Fe_2O_3(A)/FTO and α-Fe_2O_3(B)/FTO electrodes, respectively. The photocurrent density dropped in the first two cycles and then was steady and quasi-reproducible after several on–off cycles of light illumination. There was no overshoot at the beginning or at the end of the on–off cycle, meaning that the direction of the electron diffusion is free from grain boundaries, which can create traps to hinder electron movement and slow down the photocurrent generation[48].

Figure 13 shows the action spectra for the best performing α-Fe_2O_3/α-Fe_2O_3/FTO bilayer samples compared to the α-Fe_2O_3(A), α-Fe_2O_3(B) films. Significant performance gains were observed upon all throughout the illumination wavelengths. The best performing samples were α-Fe_2O_3/ α-Fe_2O_3/FTO bilayer, which had IPCEs at 400 nm of 9%, with an applied potential of 0.4V v.s Ag/AgCl. These IPCE values were 3 times higher than the α-Fe_2O_3 (A) and α-Fe_2O_3 (B) samples for the α-Fe_2O_3/ α-Fe_2O_3/FTO bilayer samples.The high energy

Journal of The Electrochemical Society, 165 (2) H1-H9 (2018)
doi. 10.1149/2.1131802jes

photons are absorbed in the outermost layers of hematite and therefore, the photogenerated holes have a shorter diffusion path to reach the surface where they will participate in oxidative chemical reaction. A positively applied potential will increase the collection efficiency of the electrons and the IPCE increases, as shown in Figure 13. Furthermore, the applied bias will facilitate hydrogen production at the Pt counter electrode by shifting its negative potential to overcome the approximately 0.4 V (vs. Ag/AgCl) difference between the hematite flat band potential and the hydrogen redox level.

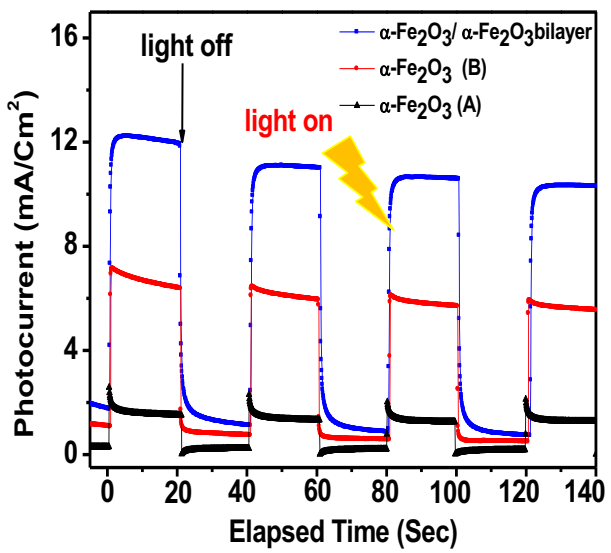

Figure 12: Photocurrent intensity for α-Fe_2O_3(A),α-Fe_2O_3(B) and α-Fe_2O_3/α-Fe_2O_3(bilayer) electrodes under successive on/off illumination cycles, measured in 1M NaOH electrolyte under a bias potential of +0.1 V.

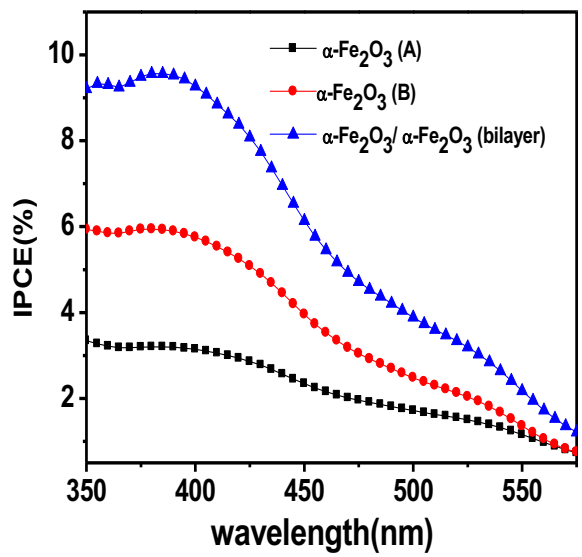

Figure 13: IPCE for α-Fe_2O_3(A),α-Fe_2O_3(B) and α-Fe_2O_3/α-Fe_2O_3(bilayer) at 0.4 V (vs. Ag/AgCl) applied potential in N_2 degassed 1 M NaOH.

3.6. Photocurrent density–voltage(J-V) of the solar cell device.

Figure 14 depicts the dark and under illumination (J–V) characteristicsof the α -Fe_2O_3(A)/α-Fe_2O_3(B)/$MAPbI_3$/Au solar cell. From the J–V curves, we can deduce open-circuit voltage (V_{oc}) and short-circuit current density (J_{sc}). These parameters are summarized in Table 2. The power conversion efficiency (η (%)) and Fill factor (FF (%)) are calculated from the following equations:

$$\mathbf{FF} = \frac{I_{max}V_{max}}{I_{sc}V_{oc}} \quad (7)$$

Journal of The Electrochemical Society, 165 (2) H1-H9 (2018)
doi. 10.1149/2.1131802jes

$$\eta(\%) = \frac{I_{sc}V_{oc}FF}{P_{input}} * 100 \quad (8)$$

where, P_{input} is the power of the incident light, I_{max} and V_{max} are the maximum current and maximum voltage,I_{sc} is the short circuit current, and V_{oc} is the open circuit potential, both can be extracted from the (J-V) curves. In the dark, the current magnitude of the cellis negligible. However, under illumination, the current magnitude of the cellincreases up promptly. The current becomes stronger and increases more rapidly. This is sincethe conductivity of α-Fe_2O_3 is improved with the incorporation of perovskite. It should be emphasized that proper perovskite can greatly enhance the separation of electron-hole pairs.

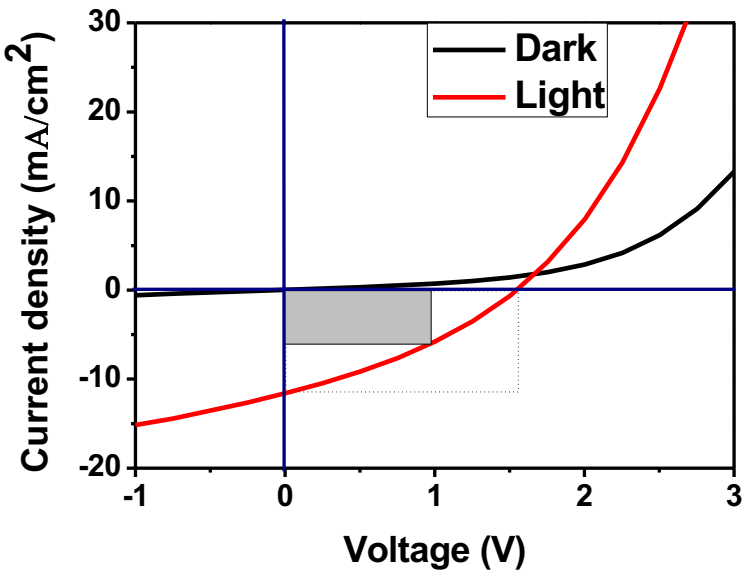

Figure 14: J-V curve solar cell devices in the dark and illumination.

Sample	*V_{oc} [V]*	*J_{sc} [mA cm^{-2}]*	*V_{max} [V]*	*J_{max} [mA cm^{-2}]*	*Fill factor [%]*	*η [%]*
Perovskite solar cells	1.55	11.27	0.99	5.7	33%	5.76%

Table 2: Photovoltaic parameters of Perovskite solarcells

4. Conclusion

In this study, we the performance ofPSCs based on α-Fe_2O_3as the electron transport material, perovskite as the light harvester, and spiroMeOTAD as the hole transporting material. The α-Fe_2O_3 thin film wasprepared by the electrodeposition and the hydrothermal processes. The perovskite layer is synthesized on the surface of the α-Fe_2O_3 thin film using the spin coating method. It was found that the growth of the α-Fe_2O_3 thin film has a clear influence on the uniform formation of theperovskite layer. Dense α-Fe_2O_3 thin films with appropriate grain sizes can ensure uniform coverage of the perovskite film, forming a better contact between the α-Fe_2O_3 film and the perovskite layer, which is able to not only facilitate the charge transport, but also to reduce charge recombination of the α-Fe_2O_3/perovskite interface.The photoelectrochemical performance of the nanostructured α-Fe_2O_3/ α-Fe_2O_3bilayer is higher than that of FTO/ α-Fe_2O_3 (A) and FTO/ α-Fe_2O_3 (B). Water splitting performance was evaluated and the highest photocurrent density of 12 mA/cm^2 v.s Ag/AgCl was exhibited for the α-Fe_2O_3/ α-Fe_2O_3bilayer photoelectrode, which had IPCEs at 400 nm of 9%, with an applied potential of 0.4V v.s Ag/AgCl.The dependence of the photovoltaic properties of PSCs on α-Fe_2O_3 is carefully examined. The stability of PSCs is also studied. The best-performing device with a PCE of 5.76%, a V_{oc} of 1.55V, a J_{sc} of 11.27 mA cm^{-2}, and a FF of 33% is demonstrated. This effect can be ascribed to the dense perovskite films that leadtofull coverage of the α-Fe_2O_3 film, forming a better contact with the α-Fe_2O_3 thin film. In addition, the best performing device is also the most stable among all the devices presented. Therefore, we can state that the contact between α-Fe_2O_3 and the perovskite layer is the critical factor that determines the photovoltaic performance of PSCs. Moreover, the results indicate the great potential of α-Fe_2O_3 as anelectron transport material, which provides high variety for perovskite-based solar cell design.

Acknowledgements

This work was supported by the Ministry of High Education and Scientific Research, Tunisia and Ministerio de Economía y Competitividad (ENE2013-46624-C4-4-R) and Generalitat valenciana (Prometeus 2014/044).

References

[1] Y. Ogomi, A. Morita, S. Tsukamoto, T. Saitho, N. Fujikawa,Q. Shen, T. Toyoda, K. Yoshino, S. S. Pandey, T. Ma and S. Hayase, J. Phys. Chem. Lett., 2014, 5, 1004.

[2] S. Kazim, M. K. Nazeeruddin, M. Gr¨atzel and S. Ahmad,Angew. Chem., Int. Ed., 2014, 53,2812.

[3] J. M. Ball, M. M. Lee, A. Hey and H. J. Snaith, Energy Environ. Sci., 2013, 6, 1739.

[4] Q. Dong, Y. Fang, Y. Shao, P. Mulligan, J. Qiu, L. Cao andJ. Huang, Science, 2015, 347, 967.

[5]A. Kojima, K. Teshima, Y. Shirai and T. Miyasaka, J. Am.Chem. Soc., 2009, 131, 6050–6051

[6]M. M. Lee, J. Teuscher, T. Miyasaka, T. N. Murakami and H. J. Snaith, Science, 2012, 338, 643–647

[7]M. Liu, M. B. Johnston and H. J. Snaith, Nature, 2013, 501, 395–398.

[8] H. Zhou, Q. Chen, G. Li, S. Luo, T.-B. Song, H.-S. Duan,Z. Hong, J. You, Y. Liu and Y. Yang, Science, 2014, 345, 542–546.

[9]W. S. Yang, J. H. Noh, N. J. Jeon, Y. C. Kim, S. Ryu, J. Seo and. I. Seok, Science, 2015, 348, 1234–1237.

[10]N.-G. Park, J. Phys. Chem. Lett., 2013, 4, 2423–2429.

[11] H. T. Peng, W. H. Sun, Y. L. Li, W. B. Yan, P. R. Yu, H. P. Zhou, Z. Q. Bian and C. H. Huang, J. Photonics Energy, 2016, 6, 022002.

[12]Q. S. Dong, Y. T. Shi, K. Wang, Y. Li, S. F. Wang, H. Zhang, Y. J. Xing, Y. Du, X. G. Bai and T. L. Ma, J. Phys. Chem. C, 2015, 119, 10212–10217.

[13] Q. Wu, W. Zhou and Q. Liu, ACS Appl. Mater. Interfaces, 2016, 8, 34464–34473.

[14]H. J. Snaith, J. Phys. Chem. Lett., 2013, 4, 3623–3630.

[15] J. H. Noh, H. I. Sang and H. H. Jin, Nano Lett., 2013, 13, 1764–1769.

[16] H.-S. Kim, C.-R. Lee, J.-H. Im, K.-B. Lee, T. Moehl,A. Marchioro, S.-J. Moon, R. Humphry-Baker, J.-H. Yum and J. E. Moser, Sci. Rep., 2012, 2, 591–598.

[17] J. H. Im, C. R. Lee and J. W. Lee, Nanoscale, 2011, 3, 4088–4093.

[18] N. J. Jeon, H. G. Lee and Y. C. Kim,J. Am. Chem. Soc., 2014, 136, 7837–7840.

[19] A. Mei, X. Li and L. Liu, Science, 2014, 345, 295–298.

[20] D. Liu and T. L. Kelly, Nat. Photonics, 2013, 8, 133–138.

[21] A. Dymshits, L. Iagher and L. Etgar, Materials, 2016, 9, 60.

[22] J. T. W. Wang, J. M. Ball and E. M. Barea, Nano lett., 2013, 14,24–730.

[23] J. M. Ball, M. M. Lee, A. Hey and H. J. Snaith, Energy Environ. Sci., 2013, 6, 1739–1743.

[24]M. J. Carnie, C. Charbonneau, M. L. Davies, J. Troughton,T. M. Watson, K. Wojciechowski, H. Snaith and D. A. Worsley, Chem. Commun., 2013, 49, 7893–7895.

[25]Q. Zhang, C. S. Dandeneau, X. Zhou and C. Cao, Adv. Mater.,2009, 21, 4087–4108.

[26]J. B. Baxter and E. S. Aydil, Appl. Phys. Lett., 2005, 86,1–3.

[27] I. Gonzalez-Valls and M. Lira-Cantu, Energy Environ. Sci.,2009, 2,19–34.

[28] L. Wang, W. F. Fu, Z. W. Gu, C. C. Fan, X. Yang, H. Y. Li andH. Z. Chen, J. Mater. Chem. C, 2014, 2, 9087–9090.

[29] D. –Y. Son, J. –H. Im, H. –S. Kim and N. –G. Park, J. Phys.Chem. C, 2014, 118, 16567–16573.

[30] M. H. Kumar, N. Yantara and S. Dharani, Chem. Commun.,2013,49, 11089–11091.

[31] H. Wang, Z. Xu, H. Yi, H. Wei, Z. Guo and X. Wang, Nano Energy, 2014, 7, 86.

[32]H. Niu, S. Zhang, Q. Ma, S. Qin, L. Wan, J. Xu and S. Miao, RSC Adv., 2013, 3, 17228.

[33]H.-S.Kim ,C.-R.Lee , J.-H. Im ,K.-B.Lee ,T.Moehl ,A.Marchioro , S.-J.Moon , R. Humphry-Baker,J-HYum ,J. E Moser , M.Grätzel N.-G.Park ,Sci. Rep.2012 , 2 , 591 .

[34] J.-Y.Jeng,Y.-F.Chiang ,M.-H.Lee, S.-R.Peng, T.-F.Guo, P.Chen, T.-C.Wen, Adv. Mater. 2013, 25, 3727.

[35] M. H.Kumar,N.Yantara,S.Dharani,M Graetzel,S.Mhaisalk P. P. Boix, N.Mathews,Chem .Commun.201,49, 11089.

[36] H.-S. Kim, J.-WLee, N.Yantar, P. P.Boi, S. A.Kulkarni, S.Mhaisalkar, M.Gratzel, N.-G.Park, Nano Lett. 2013, 13, 2412.

[37] D.Bi, S.-J.Moon, L.Häggman, G.Boschloo, LYang, E. M. JJohansson, M. K.Nazeeruddin, M. Grätzel, A. Hagfeldt,RSC Adv. 2013, 3, 18762.

[38] K.-C.Wang, J.-Y.Jeng, P.-S. Shen, Y.-C.Chang, E. W.-G. Diau, C.-H.Tsai, T.-Y. Chao, H.-C.Hsu, P.-Y.Lin, P. Chen, T.-F. Guo T.-C. Wen, Sci. Rep.2014, 4, 4756.

[39] J. A. Christians, R. C. M. Fung, P. V. Kamat, J. Am. Chem.Soc. 2014, 136, 758.

[40]L. Vayssieres, N. Beermann, S.E. Lindquist, A. Hagfeldt, Controlled aqueous chemical growth of oriented three-dimensional crystalline nanorod arrays: application to iron(III) oxides, Chem. Mater. 13 (2001) 233–235.

[41] A. Annamalai, P.S. Shinde, A. Subramanian, J.Y. Kim, J.H. Kim, S.H. Choi, J.S. Lee, J.S. Jang, Bifunctional TiO_2 underlayer for α-Fe_2O_3 nanorod based photoelectrochemical cells: enhanced interface and Ti4þ doping, J. Mater. Chem. A 3 (2015) 5007–5013.

[42] Mingyang Li,Ziyang Zhang,Feiyi Lyu,Xinjun He,Zhihao Liang,Muhammad-Sadeeq Balogun,Xihong Lu,Ping-Ping Fang,Yexiang Tong, Facile Hydrothermal Synthesis of Three Dimensional Hematite Nanostructures with Enhanced Water Splitting Performance, Electrochimica Acta, 20 December 2015 Volume 186, 20 December 2015, Pages 95-100.

[43] E.L. Miller, D. Paluselli, B. Marsen, R.E. Rocheleau, Thin Solid Films 466 (2004) 307.

[44] M.R. Belkhedkar, A.U. Ubale, International Journal of Materials and chemistry,4 (2014) 109-116.

[45] R. J. Elliott, Phys. Rev. 108, 1384 (1957)

[46] S.S. Shinde, R. A. Bansode, C. H. Bhosale, and K.Y.Rajpure, Journal of Semiconductors 32 (2011) 013001.

[47] Flavio L. Souza, Kirian P. Lopes, Pedro A.P. Nascente, Edson R. Leite, Solar Energy Materials & Solar Cells 93(2009) 362–368.

[48]M. Sookhakian, Y.M. Amin, S. Baradaran, M.T. Tajabadi, A. MoradiGolsheikh, W.J. Basirun, Thin Solid Films (2014) 204–211.